Research Square

Preprints are preliminary reports that have not undergone peer review.
They should not be considered conclusive, used to inform clinical practice,
or referenced by the media as validated information.

Three-dimensional magic angles enabled with an acoustic metacube

Tianzhi Yang

yangtianzhi@me.neu.edu.cn

Northeastern University https://orcid.org/0000-0002-8989-8990

Chenglin Han

Northeastern University

Hong-Tao Zhou

National University of Singapore https://orcid.org/0000-0002-9813-3279

Shida Fan

Northeastern University

Liang Bai

Northeastern University

Jingjing He

Beihang University

Jie Sun

Northeastern University

Cheng-Wei Qiu

Department of Electrical and Computer Engineering, National University of Singapore
https://orcid.org/0000-0002-6605-500X

Article

Keywords:

Posted Date: March 16th, 2026

DOI: https://doi.org/10.21203/rs.3.rs-8877696/v1

License: This work is licensed under a Creative Commons Attribution 4.0 International License.
Read Full License

Additional Declarations: There is **NO** Competing Interest.

Three-dimensional magic angles enabled with an acoustic metacube

Chenglin Han[1,2,3†], Hong-Tao Zhou[3,5†], Shida Fan[1†], Liang Bai[1], Menghan Li[1], Jingjing He[6], Jie Sun[4 *], Tianzhi Yang[1,2 *] and Cheng-Wei Qiu[3, *]

Affiliations

[1]*School of Mechanical Engineering and Automation, Northeastern University, 110819 Shenyang, China*

[2]*Key Laboratory of Vibration and Control of Aero-Propulsion System, Ministry of Education, Northeastern University, 110819 Shenyang, China*

[3]*Department of Electrical and Computer Engineering, National University of Singapore, 117583 Singapore, Singapore*

[4]*The State Key Laboratory of Digital Steel, Northeastern University, 110819 Shenyang, China*

[5]*Department of Mechanics, School of Mechanical Engineering, Tianjin University, 300350 Tianjin, China*

[6]*School of Reliability and Systems Engineering, Beihang University, 100191 Beijing, China*

***Email Address:** chengwei.qiu@nus.edu.sg (C.-W. Qiu); sunjie@ral.neu.edu.cn (J. Sun); yangtianzhi@me.neu.edu.cn (T. Yang).

Abstract

Hyperbolic moiré materials enable exotic band hybridization, flat-band physics and magic angles[1-4], but have so far been mostly restricted in two dimensions[5-7]. Here we introduce a nonlocal acoustic metacube architecture that lifts these intrinsic constraints and powers up a genuinely three-dimensional (3D) regime of moiré band engineering. In this 3D setting, the magic angle concept is generalized through the inequivalence of eigen-dispersion projections along three mutually orthogonal directions, enabling rich multidirectional band hybridizations that cannot occur in planar systems. As a result, the metacube stably supports multidimensional dispersion reconfiguration, flat-band formation, and asymmetric wave transport, while allowing wave propagation beyond surface confinement with pronounced out-of-plane radiation. By establishing a reconfigurable 3D nonlocal framework for moiré physics, this work defines a new regime of high-dimensional band hybridization and wave control.

Introduction

Moiré materials, formed through the twist-induced superlattice coupling of layered structures, have emerged as a versatile platform for band engineering across condensed matter physics, photonic, acoustic and elasticity[8-11]. A central phenomenon of these systems is the appearance of magic angles, where delicate interlayer coupling suppresses dispersion and gives rise to nearly flat energy bands. Although flat bands are typically associated with wave localization due to vanishing group velocity, the weakly dispersive bands in twisted systems allows for highly confined and low-loss transport of electrons, photons and other quasiparticles. It opens new opportunities for wave-based functional devices across diverse physical domains[12-18].

In recent years, moiré physics has been extended to hyperbolic polariton systems, where each constituent layer exhibits strong or even extreme anisotropy[19-22]. In such twisted bilayers, wave transport is primarily guided along the principal axis of each layer while decaying rapidly out of plane[23,24]. As the twist angle varies, the interlayer coupling leads to hybridization between the hyperbolic branches of adjacent layers, thereby continuously reshaping the dispersion topology from open hyperbolic to closed elliptical isofrequency contours. Near specific magic angles, this hybridization yields quasi-flat dispersion surface, supporting nearly stationary modes with strongly confined energy flow, suppressed radiation loss, and highly directional propagation. Such features make these systems highly promising for wave-based routing, focusing, and energy-transfer applications.

However, conventional moiré systems remain intrinsically fragile. Their planar geometry confines all interactions within interfacial planes[25,26], preventing volumetric coupling pathways. Moreover, their weak interlayer interactions limit cooperative response, hindering the formation of robust multidimensional dispersion landscapes[27,28]. In addition, existing implementations mainly rely on in-plane geometric variations or local material adjustments[29-31], providing limited

tunable degrees of freedom. As a result, the exotic effects they host, such as— flat bands, correlated states, or canalized transport— exist only within a narrow and fragile parameter space[32-35]. Such systems are inherently two-dimensional (2D), weakly coupled, and symmetry-locked, making truly programmable or multidimensional wave control fundamentally inaccessible.

Breaking away from the planar constraint, we construct a compact 3D acoustic architecture, the nonlocal metacube, designed to extends moiré physics into a higher-dimensional regime with hybrid dispersion. Each metacube module consists of a cubic unit cell containing resonant cavities and connecting channels, combined with a clip connector (Fig. 1a, b). This design allows multiple modules to be assembled into a metasurface (Fig. 1c). Subsequently, the metasurfaces, together with the connector rings mounted above their central units, are assembled to form a fully 3D reconfigurable metacube (Fig. 1d). Importantly, by reconfiguring the positions of the clip connectors and connector rings within the metacube, the twisting layer can be arbitrarily reassigned among the three orthogonal faces, rather than being fixed to a single stacking direction. This capability fundamentally distinguishes the metacube from conventional multilayer stacking architectures.

The impedance maps of the cubic unit (Fig. 1e–g) show orthogonal imaginary components with opposite or identical signs, characteristic of hyperbolic and elliptic regimes. This behavior reflects the coexistence of isotropic, anisotropic and extreme-anisotropic impedance states within a single unit. By mechanically connecting these modules, the metacube modules can also be reconfigured into a variety of 3D geometries. For instance, a stepped bulk anisotropic structure can be constructed (Fig. 1h), potentially realizing phenomena analogous to ghost hyperbolic surface polaritons[21]. When this stepped arrangement is extended along two orthogonal directions, it evolves into a pyramidal-like architecture (Fig. 1i), implying the potential for more complex

intermodal interactions. A simple 2D anisotropic metasurface can also be assembled (Fig. 1j), exhibiting a distinct hyperbolic dispersion[24]. The assembly and twisting processes of the metacube are shown in Supplementary Video S1.

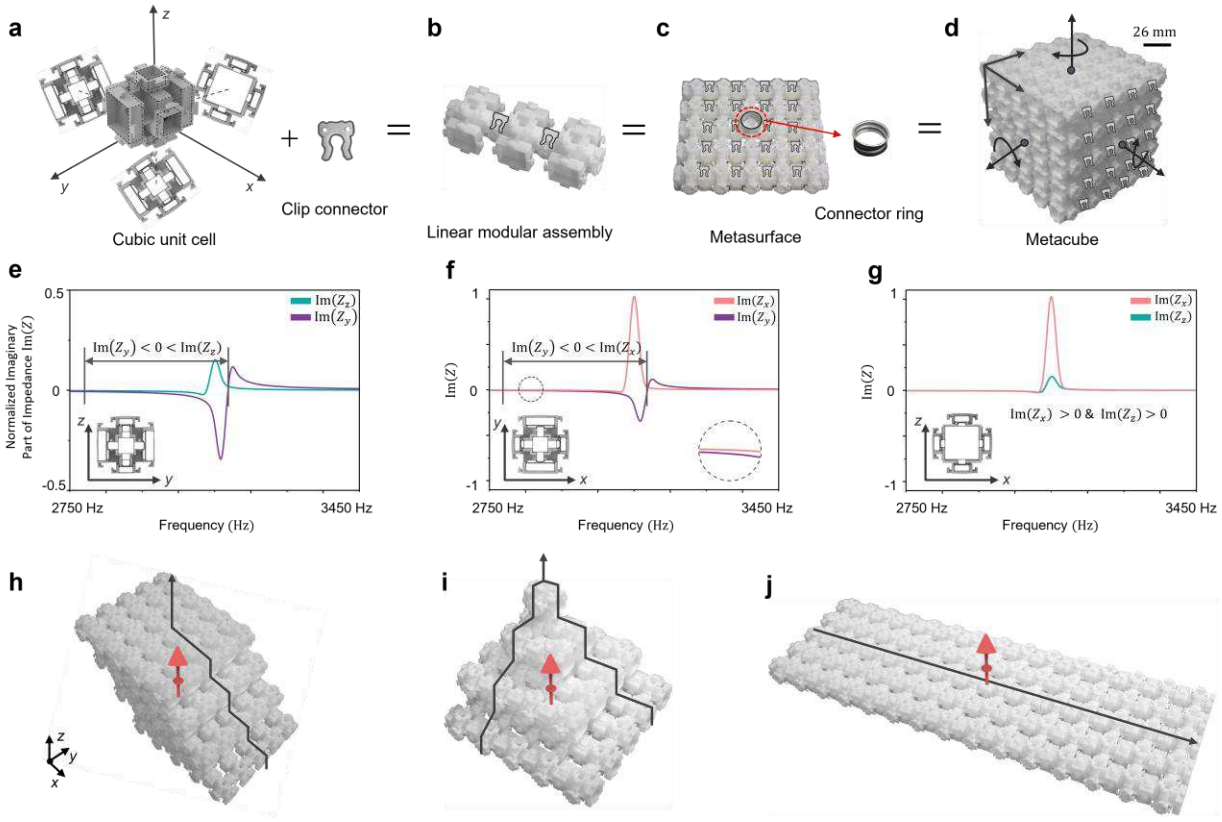

Fig. 1: Design framework of a 3D modular metamaterial architecture. a, Metacube module composed of a cubic unit cell and a clip connector. The dashed lines indicate the outline of the air domain. The three panels correspond to three mutually orthogonal cross sections taken through the center of the cubic unit cell. **b**, Linear modular assembly formed by serially connecting metacube modules. **c**, Metasurface constructed by arranging multiple linear modular assemblies arranged in a planar configuration. To enable the subsequent formation of the cube, a connector ring is mounted above the central unit of the metasurface to connect adjacent layers. **d**, Metacube assembled from modular units via connector rings, allowing mechanically twisting between layers (only one face of the clip connection is highlighted in the figure). **e-g**, Imaginary parts of the acoustic impedance along different planes, revealing distinct sign distributions associated with anisotropic (hyperbolic) and isotropic (elliptic) regimes. The inset in panel **f** highlights a magnified local segment. **h-j**, Representative reconfigurable 3D assemblies formed by mechanically

connecting metacube modules.

In contrast to moiré stacked systems, where interlayer coupling is primarily determined by the twist angle, the nonlocal metacube achieves a series of hybrid propagation behaviors. These include unidirectional and bidirectional canalization, localization–delocalization transitions, and asymmetric hyperbolic propagation. These phenomena arise from the cooperative interplay of cube rotation and coupling channel manipulation (see Fig. 2a), which together govern the coupling and hybridization of dispersion relations across orthogonal surfaces. The dynamic coupling enables each orthogonal face to independently sustain distinct propagation modes while facilitating energy transport far beyond the surface plane with pronounced out-of-plane transmission. Surprisingly, due to nonlocal coupling with adjacent anisotropic faces, even the nominally isotropic surface can also exhibit unidirectional canalization and asymmetric localization. Beyond acoustics, the principles demonstrated in this design can be extended to optical, elastic, and other wave-based systems, offering an integrated platform for multidimensional wave manipulation, information transport, and energy routing.

Nonlocal acoustic metacube

The nonlocal acoustic metacube, consisting of 125 3D-printed unit cells, with twist angles (α, β and θ) along the x, y, and z axes controlled by the distribution of clip connectors. The unit cells are interconnected through coupling tubes along three orthogonal directions, forming a nonlocal linkage network that facilitates energy exchange even between non-adjacent units[20,36,37]. By tilting these coupling tubes relative to the resonant cavities in the middle (σ and γ), adjacent cells become intentionally misaligned, creating an additional degree of freedom for structural tuning (see the lower-right inset of Fig. 2a, which represents the air domain of the unit cell). The detailed structural parameters of the cell are provided in Supplementary S2. The excitation is located at the center of

the metacube.

This acoustic metacube differs fundamentally from conventional stacked multilayer metasurface systems, which are typically limited to exploring magic angle conditions along a single dimension[38,39]. In contrast, the metacube introduces rotational and tilting degrees of freedom along all three spatial axes, enabling multidimensional coupling and band hybridization beyond the constraints of planar moiré systems. The nonlocal 3D coupling breaks the surface-bound propagation limit, establishing interconnected energy channels along the three orthogonal directions. This allows in-plane and out-of-plane modes to interact synergistically and energy exchange. When the local resonant cavities and coupling tubes form a spatial resonance chain, energy is no longer confined to a single plane but continuously transferred through nonlocal pathways inside the cube. Such 3D energy circulation strengthens the interaction among orthogonal surfaces and provides the foundation for achieving all-directional, low-loss wave transport.

The metacube exhibits a distinctive hybrid propagation regime that surpasses conventional stacked systems. In traditional layered structures, only a single optimal wave phenomenon, such as canalization[1,40], can emerge when the twist angle and interlayer coupling strength are tuned to specific values, typically confined to one spatial dimension. In contrast, a single nonlocal acoustic metacube supports three representative propagation states along orthogonal directions (triggered by 3D magic angles), including localization, canalization, and asymmetric hyperbolic transport (Fig. 2b). Remarkably, as illustrated in Fig. 2c, even a single surface of the metacube can reconfigure among four characteristic propagation modes, including an additional unidirectional canalization state.

This phenomenon originates from two intertwined factors. First, the metacube integrates three

distinct dispersion archetypes. As shown in Figs. 2d–f, the three reciprocal-space planes from left to right exhibit a smooth hyperbolic contour characteristic of extreme anisotropy, a circular profile indicative of isotropy, and a standard hyperbolic branch associated with moderate anisotropy. The coexistence of these contrasting dispersions provides a solid basis for multidimensional wave manipulation. Second, the system possesses an exceptional degree of tunability. Twist in different planes breaks the in-plane symmetry, whereas tilting introduces out-of-plane symmetry breaking. These combined distortions make the isofrequency contours asymmetric and induce hybridization among dispersive branches across orthogonal faces, collectively reshaping the global propagation landscape[11]. The synergy between unconventional hybrid dispersion and structural tunability thus establishes a new route toward multidimensional wave manipulation. For clarity, the coupling tube in the unit-cell schematic is intentionally stretched to highlight the tilt angle. Detailed isofrequency contours are provided in Supplementary S3.

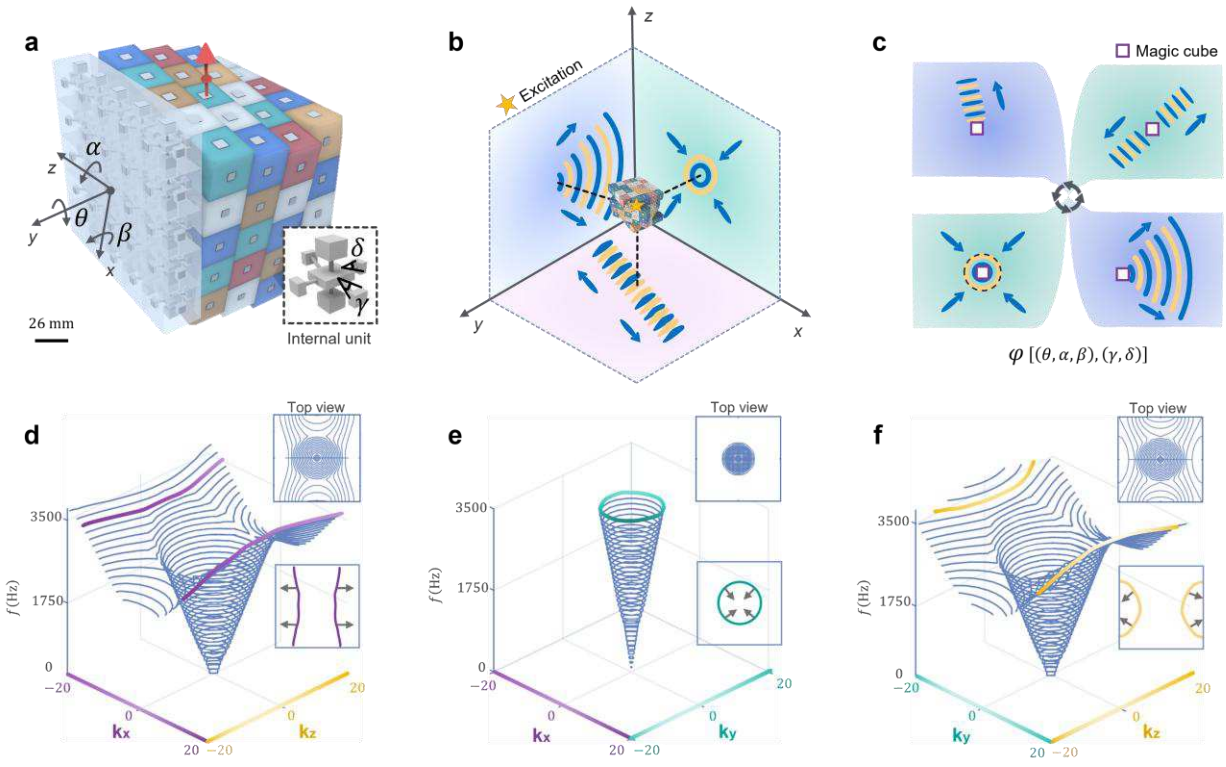

Fig. 2: Nonlocal acoustic metacube with multidimensional coupling. a, Acoustic metacube. The metacube possesses five tunable degrees of freedom: the twist angles along three orthogonal directions, as well as the coupling-region tilt angles, as illustrated in the unit cell diagram in the lower right corner. **b**, Three distinct wave propagation states in a single metacube. The wave propagation states observed on the three surfaces are asymmetric hyperbolic propagation, canalization, and localization, respectively. **c**, Four interconvertible wave propagation states. Adjusting the twist and tilt angles enables tunable transitions between unidirectional canalization, bidirectional canalization, localization and asymmetric hyperbolic propagation. **d-f**, Hybrid dispersion in the metacube. From left to right, the $k_x k_z$ plane shows smooth hyperbolic dispersion characteristic of extreme anisotropy, the $k_x k_y$ plane presents circular dispersion associated with isotropy, and the $k_y k_z$ plane exhibits typical hyperbolic dispersion arising from anisotropy.

Multidirectional dispersion hybridization

To elucidate the wave-propagation characteristics of the metacube under combined geometric modulations, we first analyze one of its orthogonal faces and construct an effective transfer-matrix model along that direction. Unlike conventional moiré systems, where geometric modulation is restricted to a single in-plane twist angle[22], the metacube employs three mutually orthogonal twist angles (θ, α and γ) together with two tilt angles (γ and δ) associated with its directional coupling channels. The twist angles alter the relative orientation of adjacent interfaces along the three axes, while the tilt angles modulate the effective propagation paths within the corresponding coupling conduits. Their combined action gives rise to a distinctly direction-dependent coupling behavior.

Under these conditions, the chosen orthogonal face can be viewed as a generalized five-layer system stacked along a specific direction. Its overall wave propagation is described by the total transfer matrix:

$$\hat{T}_{1\to n+1} = \hat{T}_{1\to 2}\hat{T}_{d_1}\hat{T}_{2\to 3}\cdots\hat{T}_{d_{n-1}}\hat{T}_{n\to n+1} \tag{1}$$

with:

$$\hat{T}_{d_n} = \begin{pmatrix} e^{ik_z d_j} & 0 \\ 0 & e^{-ik_z d_j} \end{pmatrix} \tag{2}$$

where matrix $\hat{T}_{n\to n+2}$ denotes the transfer matrix relating the input and output acoustic pressures in a monolayer, and matrix $\hat{T}_{d_j}$ corresponds to the propagation through an interlayer of thickness d_j, connecting adjacent layers. Since our metacube is designed with five layers, the overall transfer matrix is given by $\hat{T}_{1\to 5+1}$. By applying the Bloch condition, the dispersion relation along this direction is obtained. Figure 3 presents the evolution of the dispersion curves on this orthogonal face under different combinations of twist and tilt angles. The dispersion characteristics of the other two orthogonal faces can be obtained similarly by constructing transfer matrices along their directions and applying the same Bloch condition. The detailed derivation is provided in Supplementary S4.

Figure 3 summarizes the theoretical predictions of 3D band hybridization in the metacube under different combinations of twist and tilt angles. In the absence of geometric modulation, the untuned structure exhibits no interlayer hybridization with three distinct types of dispersion coexist independently within a single cube (Fig. 3a). With the introduction of a twist angle, interlayer coupling is activated and induces band hybridization, leading to a reconstruction of the dispersion curves. When the twist angle is properly adjusted, a 2D magic angle condition emerges on the anisotropic surface, enabling low-loss canalization (Fig. 3b). At this stage, the system breaks its in-plane symmetry, consistent with the underlying mechanism of conventional moiré systems[1,41]. Analogous to bulk anisotropic crystals[21,24], a tilt angle turns the hybridized surface-guided modes into ghost modes, which partly leak from the surface while partly remain guided. When the twist and tilt angles take specific combinations, the system enters a 3D magic angle condition. This change produces dispersion curves that extend out of the surface plane yet stay partially confined (Figs. 3c–e). The tilt breaks out-of-plane symmetry, generating tilted dispersion contours that enable unidirectional canalization and asymmetric propagation. Figs. 3b-e show the hybridized

dispersion on a representative hyperbolic face, and similar behavior also appears on the other anisotropic faces of the metacube. In contrast, isotropic faces exhibit negligible interlayer hybridization, with circular isofrequency surfaces and associated wave dynamics will be discussed in later sections. These observations collectively reveal the rich forms of dispersion hybridization and the diverse propagation behaviors supported by the metacube.

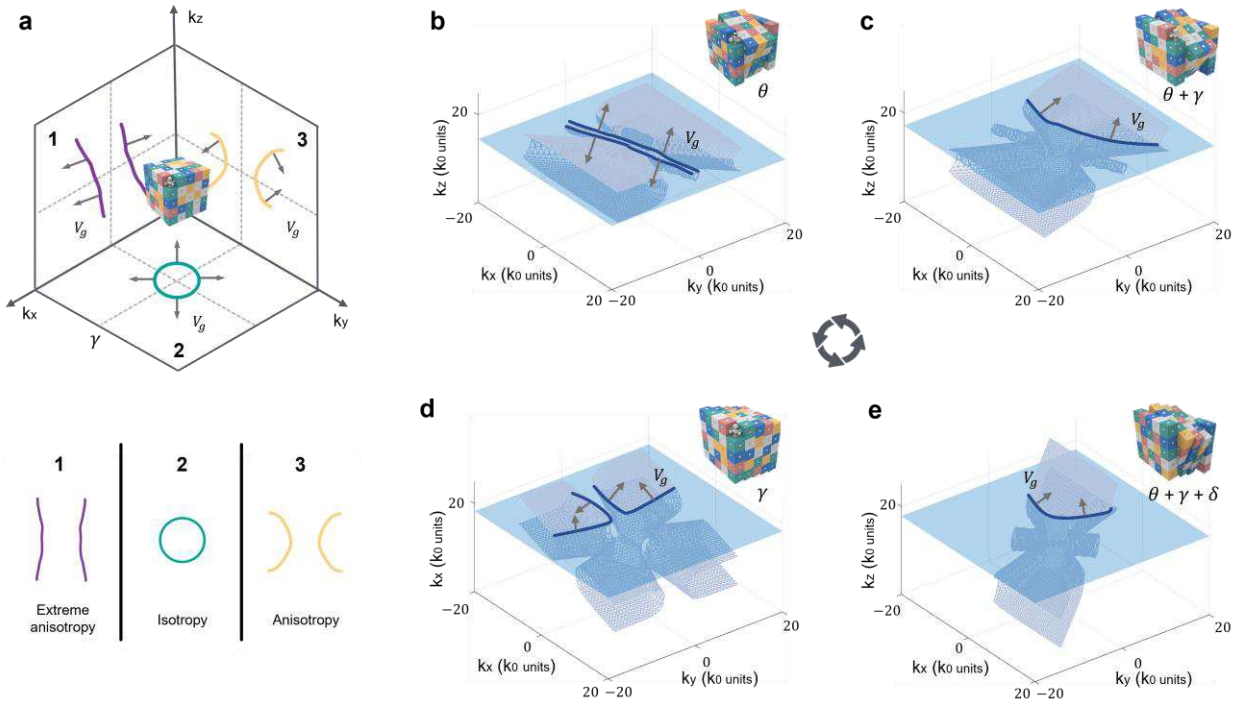

Fig. 3: Hybrid dispersion modes along different directions in metacube. a, Dispersion curves of the untwisted metacube along three orthogonal directions. The $k_x k_z$ plane shows smooth hyperbolic dispersion characteristic of extreme anisotropy, the $k_x k_y$ plane presents circular dispersion associated with isotropy, and the $k_y k_z$ plane exhibits typical hyperbolic dispersion arising from anisotropy. **b**, Flat bands are obtained by adjusting the twist angle. The group velocity is directed along two orthogonal directions, indicating low-loss canalized propagation of acoustic waves. **c-e**, The combination of twist and tilt angles enables diverse hybridization of dispersion. Tuning the tilt angle allows spatial deflection of the dispersion curve, and in conjunction with twisting, facilitates multi-angle unidirectional canalization and asymmetric propagation.

Multiple nontrivial wave propagation modes

As shown in Fig. 4a, we present a representative combination of the twist angle θ and tilt angle γ to illustrate the dispersion-tuning mechanism via band hybridization. The Fourier spectra of the xz plane (anisotropic) and the yz plane (isotropic) are shown for different parameter sets. On the anisotropic plane, when $\gamma = 0°$, tuning θ from $0°$ to $90°$ drives a topological evolution of the dispersion from hyperbolic to flat-band to elliptical. Conversely, when the twist angle is fixed at $\theta = 30°$, increasing γ from $0°$ to $30°$ produces a sequence of transitions from flat-band to hyperbolic and then to elliptical dispersion. This behavior occurs because a tilt angle distorts and reorients the dispersion curves in the untwisted metacube (see the change in the orientation of the hyperbolic contours in the row with $\theta = 0°$). As a result, the dispersion hybridization observed after twisting reflects combined symmetry breaking induced jointly by twist and tilt in the in-plane direction, in contrast to conventional dispersion transitions[30,34]. The topological interpretation is supported by crossing points among the layer-resolved dispersion branches, indicating the robustness of the underlying coupling mechanism[1,28]. The dispersion corresponding to $\theta = 30°, \gamma = 0°$ is shown in Fig. 4b(1).

Interestingly, a range of unconventional dispersion patterns appears on the nominally isotropic surface (yz plane). As shown in the lower panels of Fig. 4a, when $\theta = 0°$ and $\gamma = 10°$, $20°$, or $30°$, distinct unidirectional branches appear, indicating the onset of directed surface transport on the xy face of the metacube. This phenomenon originates from the tilt-induced breaking of out-of-plane symmetry on the yz surface. As illustrated in Extended Data Fig. 1, part of the sound waves on the xy face radiates outward through the yz surface and gradually decays, while the remaining portion continues to propagate along the xy surface[42]. This behavior is consistently observed across all cases with a non-zero tilt angle in Fig. 4a. At this stage, the role of the twist angle also departs from its conventional function of breaking in-plane symmetry alone. It further

contributes to the breaking of out-of-plane symmetry. Consequently, a fraction of the acoustic energy radiates away from the surface and decays, whereas the remaining energy remains guided along the surface. This energy-partitioning mechanism produces the asymmetric dispersion features observed for $\theta = 30°$ and $60°$, with the acoustic field at $\theta = 30°$ corresponding to Fig. 4b(3). The case of $\theta = 90°$ represents a special configuration in which the anisotropic surface becomes aligned with the yz plane, driving a transition from isotropy to extreme anisotropy. As a result, the dispersion curve collapses into a weakly dispersive band.

The metacube hosts three intrinsically different and unconventional wave modes. Unidirectional and bidirectional canalization propagation, localization-delocalization and asymmetric hyperbolic propagation are all observed to coexist within a single metacube (see Figs. 4b–d). Hybridization among the dispersion branches becomes critical, causing the wavefronts to be funneled into highly collimated transport channels and giving rise to canalized propagation. The observed localization here is analogous to Anderson localization[43,44]. It arises from the combined effects of twisting and tilting, which introduce surface disorder and lead to wave localization. Notably, these unconventional wave modes are robust and stable, as demonstrated in Extended Data Fig. 2. As the acoustic field plane is progressively displaced away from the metacube, the characteristic canalized transport and asymmetric hyperbolic propagation remain robustly preserved despite increasing field-structure separation. This observation indicates that the reported wave phenomena are not artefacts of a specific observation plane, but instead reflect the intrinsic propagation characteristics imposed by the metacube architecture. The persistence of these features further confirms the stability of the dispersion properties across the three mutually orthogonal faces, underscoring the robustness of multidirectional dispersion hybridization in the 3D nonlocal system. Specific combinations of characteristic angles across different dimensions give rise to a 3D magic

angle condition, which in turn leads to the series of nontrivial phenomena described above.

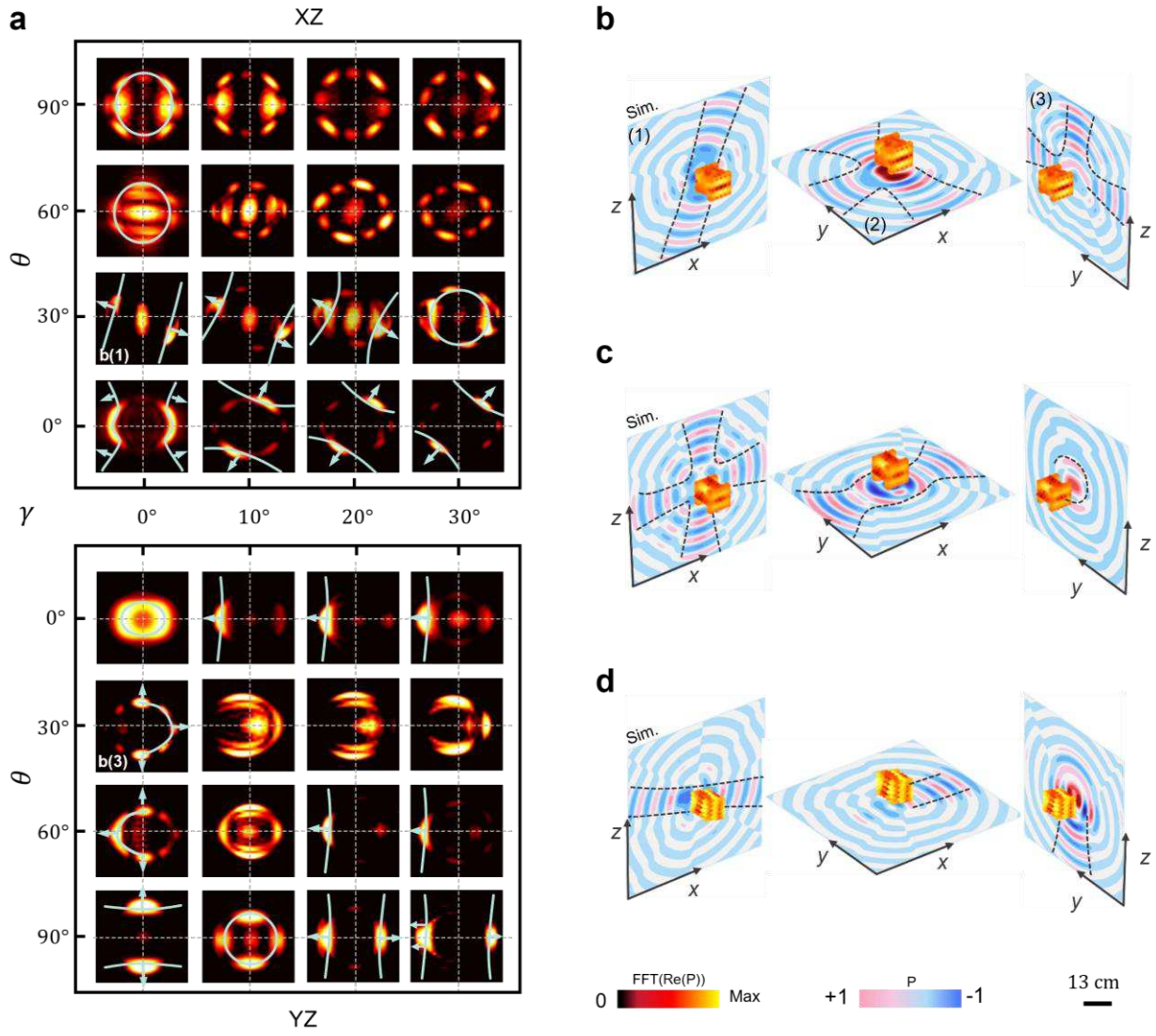

Fig. 4: Hybrid dispersion tuning and multi-modal wave manipulation in a nonlocal acoustic metacube. a, Fourier-transformed isofrequency contours of the metacube in the xz (anisotropic) and yz (isotropic) planes under various combinations of twist angle θ and tilt angle γ. The transition from hyperbolic to flat to elliptical dispersion in the anisotropic plane, and unidirectional features in the isotropic plane, reflect hybrid dispersion tuning. **b-d**, Sound pressure fields on three orthogonal planes (xz, xy, yz) for three representative configurations, illustrating canalization and asymmetric hyperbolic propagation, hyperbolic propagation and localization as well as

canalization and unidirectional propagation.

Another major advantage of the metacube is that the acoustic field extends well beyond the structure itself (Extended Data Fig. 3d), unlike conventional metasurfaces where wave propagation is confined strictly to the surface (Extended Data Fig. 3a-c). This unique behavior arises from the fully 3D nonlocal coupling network, which collectively pools, redistributes, and reuses energy stored in each unit cell throughout the structure, instead of dissipating it within a single surface layer. Beyond the results shown in Fig. 4, we systematically applied various combinations of twisting and tilting to fully map the remaining configurations. Additional acoustic field results are provided in Supplementary S5.

In addition, multiple metacubes can be modularly combined to construct a wide range of structural layouts tailored to specific functional requirements. For example, ultra-long-distance canalization can be realized by cascading metacubes along a desired direction, while more complex energy distributions or propagation behaviors can be achieved through arrangements such as quasicrystalline configurations. Such on-demand assembly enables large-scale and finely tunable control of wave transport, substantially extending the metacube's potential in both physical and engineering applications. Acoustic field results for various metacube combinations are provided in Supplementary S6.

We fabricated 125 individual metamaterial unit cells using 3D printing and assembled them into a $5 \times 5 \times 5$ metacube (Fig. 5a). The top view after twisting is shown in the central panel of Fig. 5a, where the white dashed lines mark the twisted layers, the red dashed lines indicate the untwisted layers, and the sound source is placed at the center. The unit-cell configurations differ along the three orthogonal directions, leading to distinct acoustic impedances (Fig. 5a, right; Fig. 1d–f). Figure 5b presents the cross-sectional view of the xy plane after applying twist or tilt tuning. In

this plane, both operations break the in-plane symmetry and enable effective dispersion tailoring. The red-highlighted regions indicate how the tuning modifies the geometry of the air domain within each unit.

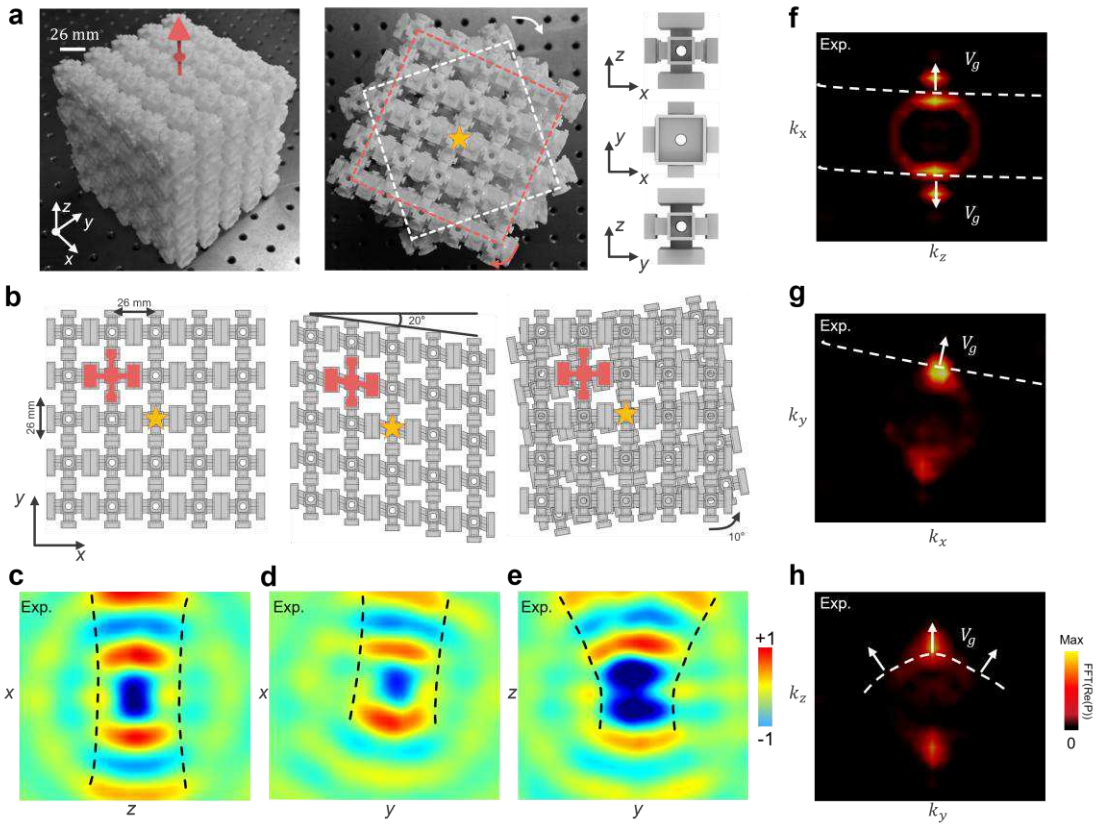

Fig. 5: Geometric structure and acoustic field distribution of the metacube. a, Overall structure of the metacube (left), its appearance after twisting (middle), and the corresponding unit-cell geometries along the three orthogonal directions (right). For clarity, the connector structures used for mechanical assembly have been removed in the unit-cell illustrations to better reveal the coupling-channel variations. **b**, Cross-sectional views of the xy plane. Red-highlighted regions indicate how tuning modifies the air-domain geometry within each unit. **c–e**, Measured acoustic pressure fields on the xz, xy, and yz planes ($f = 3645\text{Hz}$, $\beta = 15°$ and $\delta = 30°$). **f–h**, Corresponding FFT spectra.

The metacube was then placed inside a custom-designed triaxial measurement platform to characterize its acoustic response. The sound-field measurements on the metacube's three

orthogonal faces were performed at $f = 3645\text{Hz}$, with $\beta = 15°$ and $\delta = 30°$. Details of the experimental setup and measurement procedures are provided in Supplementary S7 and the Methods section. As shown in Figs. 5c–h, the measured pressure fields and the corresponding fast Fourier transform (FFT) spectra reveal three characteristic propagation behaviors. In Fig. 5c, the pressure field exhibits a pronounced canalization effect, with acoustic energy confined along a single lattice direction and minimal transverse spreading. Fig. 5d demonstrates the unidirectional canalization behavior, where wave propagation is strongly favored in one direction while being suppressed in the opposite direction. In Fig. 5e, the pressure field spreads along two oblique directions, forming an asymmetric hyperbolic transport pattern characteristic of highly anisotropic dispersion. These spatial features are consistently reflected in the corresponding FFT spectra shown in Figs. 5f–h. Concentrated spectral components aligned with a single axis are observed for canalization, whereas the unidirectional case exhibits a strongly asymmetric spectral distribution. For the hyperbolic transport regime, the FFT spectrum displays an open and asymmetric contour, in agreement with the experimentally observed wavefront patterns. These observations are in good agreement with the theoretical predictions, thereby supporting the proposed metacube design and its reconfigurable wave-transport characteristics at 3D magic angles.

Conclusion

In summary, we demonstrate a nonlocal acoustic metacube that lifts the intrinsic planar constraint of moiré systems and establishes a genuinely 3D framework for moiré band engineering. The metacube hosts three mutually orthogonal surfaces with isotropic, anisotropic, and extreme-anisotropic dispersion characteristics. By jointly tuning multiple twist and tilt angles, we realize a 3D magic angle condition, giving rise to hybrid-dispersion phenomena governed by 3D nonlocal coupling and enabling highly reconfigurable wave-propagation modes, including localization,

bidirectional and unidirectional canalization, and asymmetric hyperbolic transport, while allowing waves to escape surface confinement. These distinct propagation modes can coexist and continuously transform within a single metacube, highlighting its intrinsically multidimensional controllability. By engineering unit-cell geometries and incorporating twist modulation, precise dispersion control is achieved along all three spatial directions, leading to broadband delocalized-to-localized transitions and symmetry-breaking–induced asymmetric localization. Together, these results establish the metacube as a versatile 3D nonlocal platform that generalizes the magic angle concept beyond planar systems and enables high-dimensional band hybridization and wave-transport control, with potential extensions to other wave systems.

References

[1] Hu, G., Ou, Q., Si, G., Wu, Y., Wu, J., Dai, Z., Krasnok, A., Mazor, Y., Zhang, Q., Bao, Q., Qiu, C., Alù, A. Topological polaritons and photonic magic angles in twisted α-MoO_3 bilayers. Nature 582, 209-213 (2020).

[2] Zhang, Q., Hu, G., Ma, W, Alù, A., Qiu, C. Interface nano-optics with van der Waals polaritons. Nature 597, 187–195 (2021).

[3] Yves, S., Alù, A. Twist-induced hyperbolic shear metasurfaces. Phys. Rev. X 14, 021031 (2024).

[4] Han, C., Fan, S., Zhou, H., Yang, T., Qiu, C. All-angle unidirectional flat-band acoustic metasurfaces. Nat. Commun. 16, 634 (2025).

[5] Yves S., Peng Y., Alù A. Broadband topological transitions in twisted elastodynamic metasurfaces, Proc. Natl. Acad. Sci. U.S.A. 122(42)e2427049122 (2025).

[6] Xu, J., Yu, K., Ni, X., Alù A., Jiang T. Dynamic tuning of Bloch modes in anisotropic phonon polaritonic crystals. Light Sci Appl 15, 41 (2026).

[7] Yankowitz, M., Jung, J., Laksono, E, Dean., C. Dynamic band-structure tuning of graphene moiré superlattices with pressure. Nature 557, 404–408 (2018)

[8] Park, J., Sun, S., Jarillo-Herrero,P. ,Experimental evidence for nodal superconducting gap in moiré graphene. Science 391, 79-83 (2026).

[9] Pierce, A., Xie, Y., Jarillo-Herrero, P., Yacoby, A. Unconventional sequence of correlated Chern insulators in magic-angle twisted bilayer graphene. Nat. Phys. 17, 1210-1215 (2021).

[10] Li, M., He, K., Ren, Z., Chen, L., Dong, H., Han, C., Yang, T. and Qiu, C. Twist-on-twist moiré elastic metasurfaces. Phys. Rev. Lett. 135, 126301 (2025).

[11] Han, C., Chen, LQ., Yang, T. Alù, A., Qiu, C. Observation of dispersive acoustic quasicrystals. Nat. Commun. 16, 1988 (2025).

[12] Balents, L., Dean, C.R., Efetov, D.K., Young, A.F., Superconductivity and strong correlations in moiré flat bands. Nat. Phys. 16, 725-733 (2020).

[13] Bai, L., Yao, H., Han, C., Jing, X., Chen, L., Vakakis, A.F., Yang, T., Recent advances in nonlinear vibration metamaterials, Mechanical Systems and Signal Processing, 236, 113046 (2025).

[14] Yi, C.-H., Park, H. C., Park, M. J. Strong interlayer coupling and stable topological flat bands in twisted bilayer photonic moiré superlattices. Light-Sci Appl. 11, 289 (2022).

[15] Liu, X., Chiu, C., Lee, J., Farahi, G., Watanabe, K., Taniguchi, T., Vishwanath, A., Vishwanath, A., Spectroscopy of a tunable moiré system with a correlated and topological flat band. Nat. Commun. 12, 2732 (2021).

[16] Dong, K., Zhang, T., Li, J., Yao, Jie., Flat bands in magic-angle bilayer photonic crystals at small twists. Phys. Rev. Lett. 126, 223601 (2021).

[17] Peotta, S., Törmä, P., Superfluidity in topologically nontrivial flat bands. Nat. Commun. 6, 8944 (2015).

[18] López M., Peñaranda F., Christensen J., San-Jose Q., Flat bands in magic-angle vibrating plates, Phys. Rev. Lett., 125, 214301, 2020.

[19] Liu, L., Xiong, L., Wang, C. Hu, G. Long-range hyperbolic polaritons on a non-hyperbolic crystal surface. Nature 644, 76–82 (2025).

[20] Quan, L., Alù, A. Hyperbolic sound propagation over nonlocal acoustic metasurfaces. Phys. Rev. Lett. 123, 244303 (2019).

[21] Ma, W., Hu, G., Hu, D., Chen, R., Sun, T., Zhang, X., Dai, Q., Zheng, Y., Alù, A., Qiu, C., Li, P. Ghost hyperbolic surface polaritons in bulk anisotropic crystals. Nature. 596, 362-366 (2021).

[22] Kotov, O., Lozovik, Y. Hyperbolic hybrid waves and optical topological transitions in few-

layer anisotropic metasurfaces. Phys. Rev. B. 100, 165424 (2019).

[23] Oudich, M., Kong, X., Zhang, T., Qiu, C., Jing, Y. Engineered moiré photonic and phononic superlattices. Nat. Mater. **23**, 1169–1178 (2024).

[24] Hu, G., Ma, W., Hu, D., Wu, J., Zheng, C., Liu, K., Zhang, X., Ni, X., Chen, J., Zhang, X., Dai, Q., Caldwell, J., Paarmann, A., Alù, A., Li, P., Qiu, C. Real-space nanoimaging of hyperbolic shear polaritons in a monoclinic crystal. Nat. Nanotechnol. 18, 64-70 (2023).

[25] Chen, M., Lin, X., Dinh, T., Zheng, Z., Shen1, J., Ma, Q., Chen, H., Jarillo-Herrero, P., Dai, S. Configurable phonon polaritons in twisted α-MoO_3. Nat. Mater. 19, 1307 (2020).

[26] Huang, T., Tu, X., Shen, C., Zheng, B., Wang, J., Wang, H., Khaliji, K., Park, S., Liu, Z., Yang, T., Zhang, Z., Shao, L., Li, X., Low, T., Shi, T. & Wang, X. Observation of chiral and slow plasmons in twisted bilayer graphene. Nature 605, 63–68 (2022).

[27] Yves, S., Peng, Y., Alù, A. Topological Lifshitz transition in twisted hyperbolic acoustic metasurfaces. Appl. phys. Lett. 121, 122201 (2022).

[28] Min Park, J., Cao, Y., Jarillo-Herrero, P. Tunable strongly coupled superconductivity in magic-angle twisted trilayer graphene. Nature 590, 249–255 (2021).

[29] Călugăru, D., Jiang, Y., Hu, H., Bernevig, B. Moiré materials based on M-point twisting. Nature 643, 376–381 (2025).

[30] Yves, S., Ruzzene, M., Alù, A. Moiré-driven topological transitions and extreme anisotropy in elastic metasurfaces. Adv. Sci. 9, 2200181 (2022).

[31] Qu, Y., Hu, H., Dai, Q., Tunable planar focusing based on hyperbolic phonon polaritons in α-MoO3. Adv. Mater. 34, 2105590 (2022).

[32] Duan J., Nikitin, A. Y., Alonso-González, P. Multiple and spectrally robust photonic magic angles in reconfigurable α-MoO_3 trilayers. Nat. Mater. 22, 867–872 (2023).

[33] Hu, G., Krasnok, A., Mazor, Y., Qiu, C., Alù, A. Moiré hyperbolic metasurfaces. Nano. Lett. 20, 3217-3224(2020).

[34] Tarnopolsky, G., Kruchkov, A.J., Vishwanath, A., Origin of magic angles in twisted bilayer graphene. Physical Review Letters. 122, 106405 (2019).

[35] Krishna Kumar, R., H. L. Koppens, F., Terahertz photocurrent probe of quantum geometry and interactions in magic-angle twisted bilayer graphene. Nat. Mater. (2025).

[36] Yao, J., Lai, F., Fan, Y., Tsai, D. Nonlocal meta-lens with Huygens' bound states in the continuum. Nat. Commun.15, 6543 (2024).

[37] Overvig, A., Mann, S.A., Alù, A. Spatio-temporal coupled mode theory for nonlocal metasurfaces. Light Sci. Appl. 13, 28 (2024).

[38] Patterson, C.L., Sheekey, O.I., Arp, T.B., Young A. Superconductivity and spin canting in spin–orbit-coupled trilayer graphene. Nature 641, 632–638 (2025).

[39] Xia, LQ., de la Barrera, S.C., Uri, A., Jarillo-Herrero, P. Topological bands and correlated states in helical trilayer graphene. Nat. Phys. 21, 239–244 (2025).

[40] Dai, Z., Hu, G., Si, Qiu, C., Bao, Q. Edge-oriented and steerable hyperbolic polaritons in anisotropic van der Waals nanocavities. Nat. Commun. 11, 6086 (2020).

[41] Zhou, H., Wang, Y., Wang, Y., Qiu, C. Dynamic acoustic beamshaping with coupling-immune moiré metasurfaces. Adv. Mater. 36, 2313004 (2024).

[42] Ni, X., Carini, G., Ma, W., Maria Renzi, E., Galiff, E., Wasserroth, S., Wolf, M., Peining, L., Paarmann, A., Alù, A. Observation of directional leaky polaritons at anisotropic crystal interfaces. *Nat. Commun.* 14, 2845-2853 (2023).

[43] Schwartz T., Bartal G., Segev M. Transport and Anderson localization in disordered two-dimensional photonic lattices. *Nature* 446, 52–55 (2007).

[44] Segev M., Silberberg Y., N. Christodoulides D. Anderson localization of light. *Nat. Photonics* 7, 197–204 (2013).

Methods

Numerical simulations

Simulations were conducted in COMSOL Multiphysics using frequency-domain and eigenfrequency solvers within the pressure-acoustics module. The governing equation is

$$\nabla \cdot \left(-\frac{1}{\rho_c}\nabla p_t - \boldsymbol{q}_d\right) - \frac{k_{eq}^2}{\rho_c} p_t = Q_m$$

where $p_t = p_s + p_b$ refers to the total pressure, consisting of the scattering pressure p_s and the background pressure p_b; the parameters $\rho_c = \rho$ and $c_c = c$ correspond to the density and the sound velocity of the medium, respectively. The equivalent wave number is defined as $k_{eq}^2 =$

348 ω^2/c_c^2. The term $\boldsymbol{q}_d$ represents loss mechanisms related to acoustic dissipation, while Q_m serves
349 as the external acoustic source. The cavity boundaries were treated as acoustically rigid, enforcing
350 zero normal velocity conditions. Periodic (Bloch) boundary conditions were imposed on the lateral
351 faces of the unit cell, while perfectly matched layers (PMLs) were applied to the top and bottom
352 to absorb outgoing waves. The band structure of the crystal unit was calculated using the
353 eigenfrequency solver through a frequency sweep, as shown in Supplementary Fig. S2. To further
354 suppress boundary reflections, eight PML regions were strategically placed around the bilayer
355 moiré configuration.
356

357 ## Fabrication and experimental setup

358 Spatially resolved acoustic measurements were carried out using a scanning microphone system.
359 An acoustic microphone mounted on a motorized high-precision scanning arm was positioned
360 above the sample to record the transmitted sound pressure field over a two-dimensional region,
361 with a spatial sampling interval of 8 mm. To ensure temporal consistency across all measurements,
362 a reference microphone was placed approximately 30 cm below the excitation source to monitor
363 the incident wave field. The metacube sample was fabricated via 3D printing using R4600 resin
364 and assembled into a cubic structure composed of a $5 \times 5 \times 5$ array of unit cells. Acoustic
365 excitation was provided by a miniature loudspeaker with a radius of 3.0 mm, which was located at
366 the geometric center of the cube and operated as an approximately omnidirectional point source.
367 To suppress undesired reflections from the surroundings, acoustic foam was arranged around and
368 beneath the metacube. The experimental platform consisted of a control computer, a power
369 amplifier, two microphones, a data-acquisition chassis, a motorized motion controller, a signal
370 generator, a custom-built triaxial positioning stage, and a dedicated microphone support rod.

Additional details of the experimental apparatus are provided in Supplementary Section S7.

Acknowledgements

T.-Z.Y., acknowledge support from the National Natural Science Foundation of China [Grant No. 12232014], the Natural Science Foundation of China [Grant No. 12072221], the Fundamental Research Funds for the Central Universities [Grant No. 2013017] and the Ten Thousand Talents. C.-L.H. acknowledges the support of China Scholarship Council [Grant No. 202406080122] and the Fundamental Research Funds for the Central Universities [Grant No. N2403003]. J.-J.H acknowledges the support of the National Natural Science Foundation of China, No. U2230204 and 52575607. H.-T.Z. acknowledges the support of the Postdoctoral Fellowship Program of CPSF [GZB20240526] and the China Postdoctoral Science Foundation [2025M771871, 2025T180529). C.-W.Q. acknowledges financial support from the Ministry of Education, Singapore (Grant No. A-8000107-01-00).

Ethics declarations

The authors declare that they have no competing interests.

Author contributions

C.-W.Q., T.-Z.Y. J.S. conceived the idea. C.-L.H. and S.-D.F. performed the experiments. C.-L.H. carried out the theoretical analysis and simulations. C.-L.H. and H.-T.Z. wrote the manuscript with contributions from the other authors. All authors have made a substantial contribution to the concept and preparation of the paper.

Supplementary Information

Supporting Information is available from the corresponding authors upon reasonable request.

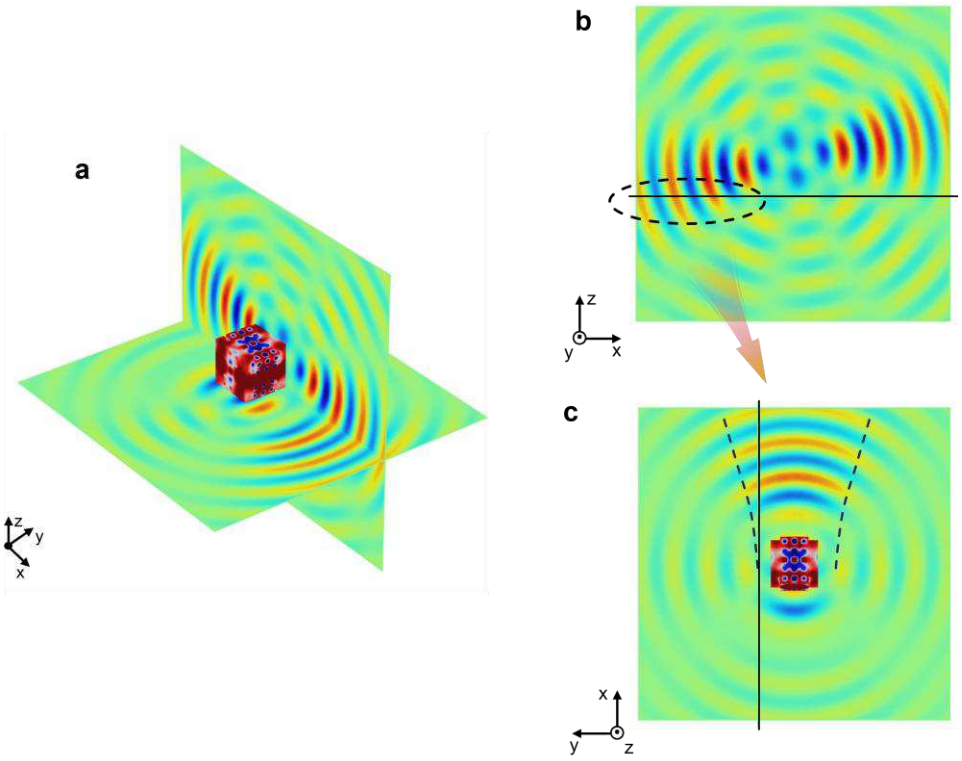

Extended Data Fig. 1: Surface radiation and directional wave propagation on the metacube. **a**, Acoustic field distribution on orthogonal planes surrounding the metacube. **b**, Acoustic field on the yz plane. The dashed ellipse indicates the region on the xy surface where the sound waves radiate, and the corresponding right-hand portion on the yz plane shows the outward and gradually decaying waves. **c**, Acoustic field on the xy plane. Because part of the energy is radiated away through the yz surface, the remaining surface wave on the xy face becomes directionally biased, producing a unidirectional propagation pattern.

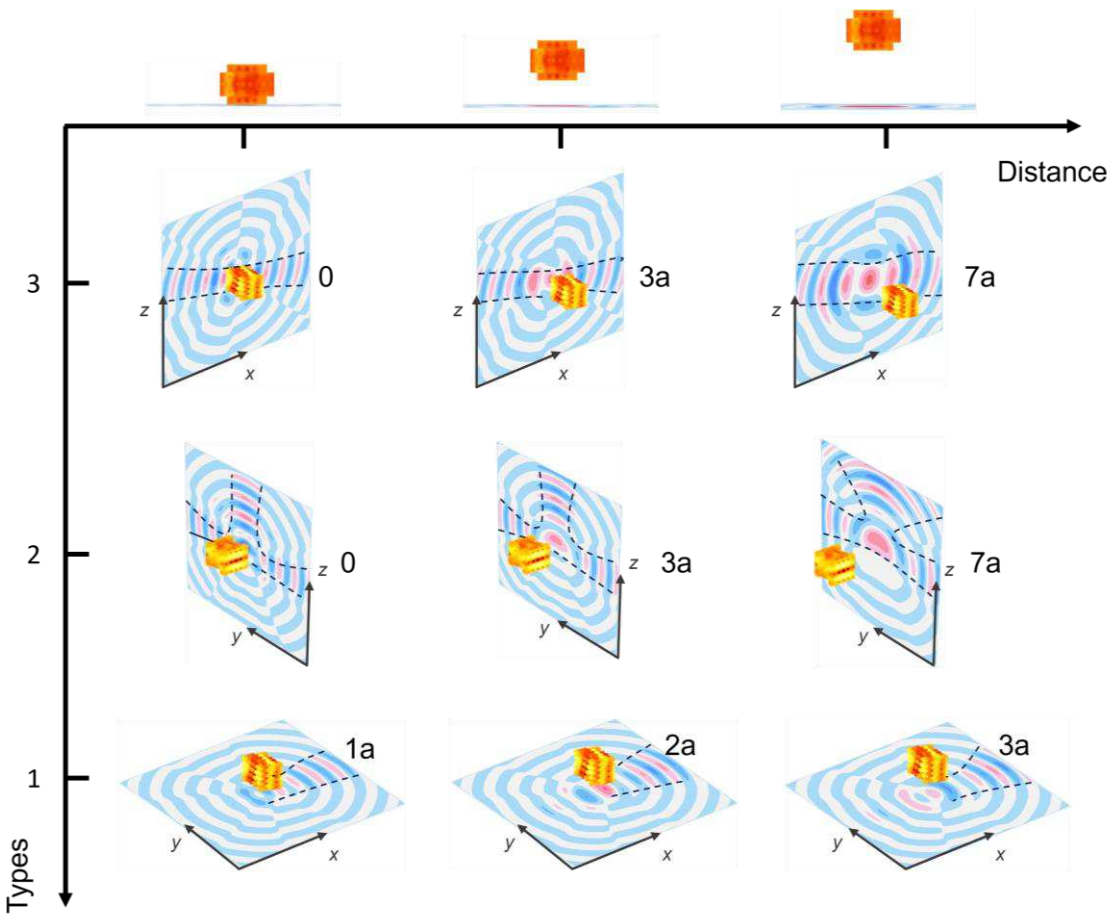

Extended Data Fig. 2: Robustness of nontrivial wave modes against observation-plane displacement. Spatial evolution of three representative wave-field distributions measured on planes displaced away from the metacube. For increasing separations (0, 1a, 2a, 3a and 7a), the overall wave propagation patterns show no noticeable change, demonstrating the stability of the dispersion characteristics across the three mutually orthogonal faces.

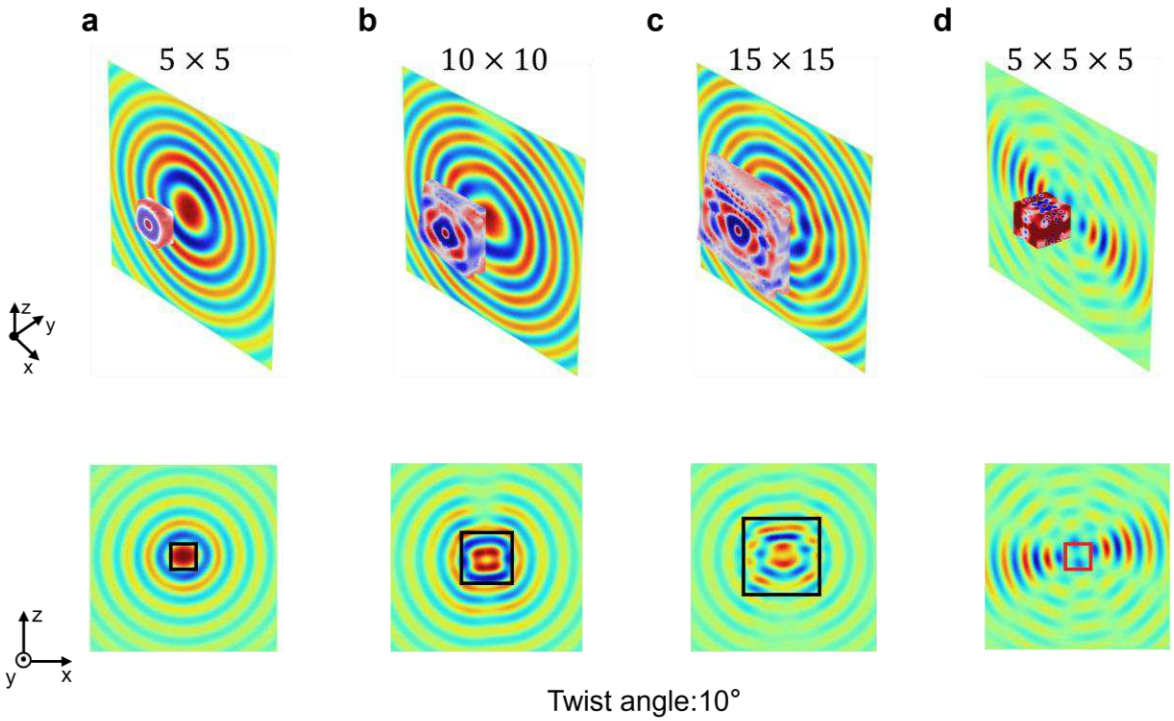

Extended Data Fig. 3: Comparison between moiré metasurfaces of different array sizes and the metacube under a fixed twist angle (10°). a-c, Acoustic field patterns for moiré metasurfaces composed of 5×5, 10×10, and 15×15 unit cells, respectively. Under the hyperbolic excitation frequency, although the number of unit cells in the metasurface increases (i.e., the resolution improves), the wave directionality remains indistinct, and this blurred behavior rapidly disappears outside the plane. **d**, Acoustic field patterns for metacube composed of $5 \times 5 \times 5$ unit cells. Clear directional transport that extends out of the plane. The bottom row shows the corresponding xy-plane fields, with the black boxes representing the metasurface above.

Supplementary Files

This is a list of supplementary files associated with this preprint. Click to download.

- Supplementmaterials.docx